Structural and Thermodynamic Analysis of HIV-1 Fusion Inhibition Using Small gp41 Mimetic Proteins

Samuel Jurado[1], Mario Cano-Muñoz[1], Bertrand Morel[1], Sara Standoli[1], Elisabetta Santarossa[1], Christiane Moog[3], Sylvie Schmidt[3], Géraline Laumond[3], Ana Cámara-Artigas[2] and Francisco Conejero-Lara[1]

1 - Departamento de Química Física e Instituto de Biotecnología, *Facultad de Ciencias, Universidad de Granada, 18071 Granada, Spain*
2 - Department of Chemistry and Physics, *Agrifood Campus of International Excellence (ceiA3) and CIAMBITAL, University of Almería, Carretera de Sacramento, 04120 Almeria, Spain*
3 - INSERM U1109, *Fédération de Médecine Translationnelle de Strasbourg (FMTS), Université de Strasbourg, Strasbourg, France*

Correspondence to Francisco Conejero-Lara: *conejero@ugr.es*
https://doi.org/10.1016/j.jmb.2019.06.022
Edited by Eric O. Freed

Abstract

Development of effective inhibitors of the fusion between HIV-1 and the host cell membrane mediated by gp41 continues to be a grand challenge due to an incomplete understanding of the molecular and mechanistic details of the fusion process. We previously developed single-chain, chimeric proteins (named covNHR) that accurately mimic the N-heptad repeat (NHR) region of gp41 in a highly stable coiled-coil conformation. These molecules bind strongly to peptides derived from the gp41 C-heptad repeat (CHR) and are potent and broad HIV-1 inhibitors. Here, we investigated two covNHR variants differing in two mutations, V10E and Q123R (equivalent to V38E and Q40R in gp41 sequence) that reproduce the effect of HIV-1 mutations associated with resistance to fusion inhibitors, such as T20 (enfuvirtide). A detailed calorimetric analysis of the binding between the covNHR proteins and CHR peptides (C34 and T20) reveals drastic changes in affinity due to the mutations as a result of local changes in interactions at the site of T20 resistance. The crystallographic structure of the covNHR:C34 complex shows a virtually identical CHR–NHR binding interface to that of the post-fusion structure of gp41 and underlines an important role of buried interfacial water molecules in binding affinity and in development of resistance against CHR peptides. Despite the great difference in affinity, both covNHR variants demonstrate strong inhibitory activity for a wide variety of HIV-1 strains. These properties support the high potential of these covNHR proteins as new potent HIV-1 inhibitors. Our results may guide future inhibition approaches.

Introduction

The HIV-1 envelope protein (Env) promotes viral entry to the host cell through membrane fusion [1,2]. Env is a non-covalently associated trimer of heterodimers of two glycoprotein subunits, gp120 and gp41 [3–5]. In native Env, the three highly glycosylated gp120 subunits occlude most of the transmembrane gp41 subunits, which are locked in a metastable conformation. Gp41 consists of an external domain (ectodomain), a transmembrane region and a C-terminal intracytoplasmic tail (Fig. 1). The ectodomain is, in turn, composed of an N-terminal, hydrophobic fusion peptide (FP), followed by a polar region, an N-terminal heptad repeat (NHR), a disulfide-bridged loop region, a C-terminal heptad repeat (CHR) and a membrane-proximal external region (MPER).

Binding of gp120 to the CD4 cell receptor followed by a subsequent binding to a chemokine coreceptor (CCR5 or CXCR4) triggers a series of large conformational changes in gp41 that finally lead to membrane fusion and insertion of the viral content into the cell cytoplasm [2,6]. In this process, gp41 forms first an extended intermediate (known as the pre-hairpin intermediate), in which the FP is inserted into the cell membrane and the NHR and CHR regions become transiently exposed. Subsequently,

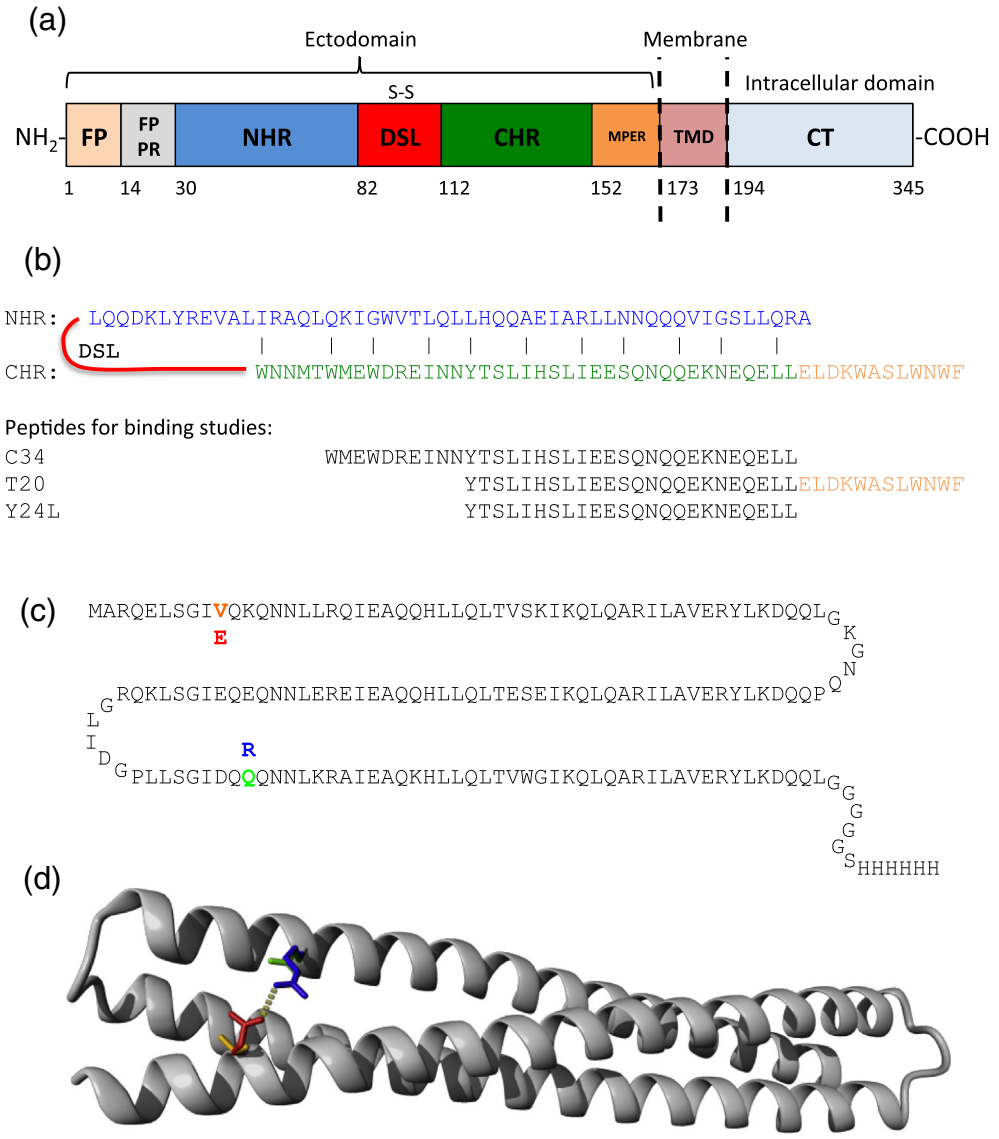

Fig. 1. Gp41 organization and protein and peptide sequences used in this work. (a) Schematic representation of gp41 functional regions. The residue numbers defining each region correspond to gp41 sequence numbers. FP, fusion peptide; FPPR, fusion-peptide proximal region; NHR, N-terminal heptad repeat; DSL, disulfide-bonded loop; CHR, C-terminal heptad repeat; MPER, membrane-proximal external region; TMD, transmembrane domain; CT, cytoplasmic tail. (b) Reference sequences (Swiss-Prot entry sp.|P03377|ENV_HV1BR) of NHR (blue), CHR (green) and MPER (Orange) regions used in this study. The NHR sequence has been reversed to illustrate the approximate NHR–CHR interactions in the post-fusion hairpin structure. (c) Amino acid sequence of covNHR proteins. Mutated residues have been highlighted next to the sequence positions. (d) Ribbon model of the covNHR structure with the mutated side chains represented in sticks and colored in orange (Val10), red (Glu10), green (Gln123) and blue (Arg123).

an energetically favorable folding of the CHR regions onto a trimer of NHR helices forms a highly stable six-helix bundle (6HB), coiled-coil structure [7,8]. This process brings the viral and cell membranes into close proximity facilitating fusion.

Due to its key role in the HIV fusion process, the gp41 pre-hairpin intermediate has become a subject of intense research during the last three decades as an attractive target for HIV-1 inhibition. In this state, both NHR and CHR regions of gp41 can be recognized by a variety of molecules, collectively known as fusion inhibitors or entry inhibitors [9], which interfere with the formation of the 6HB. Fusion inhibitors have been grouped in different classes, according to their specific target region in gp41. Class-1 inhibitors interact with hydrophobic grooves exposed by a trimeric coiled-coil of NHR helices and compete with the internal CHR region of gp41. This class includes CHR peptide mimetics [1,10–12], artificial D-peptides [13], small compounds [14,15]

and antibodies [16,17]. A prominent feature observed for most class-1 inhibitors is that they establish well-defined hydrophobic contacts with a highly conserved, deep pocket on the surface of the trimer of NHR helices [18]. For this reason, this pocket continues to serve as a promising target for development of small-molecule entry inhibitors [19].

The only FDA-approved class-1 inhibitor for treatment of AIDS/HIV patients is T20 (enfuvirtide), a peptide mimetic corresponding to gp41 residues 127–162 [10] spanning the second half of the CHR and the beginning of the MPER. Because T20 lacks the residues that interact with the hydrophobic pocket, it has a limited inhibitory potency. Moreover, T20 has other limitations for clinical use, such as a short half-life implying high dosage by twice-a-day subcutaneous injection, diverse side effects, high cost and rapid appearance of resistance [20]. Acquisition of resistance in patients under T20 treatment is produced by mutations at the sequence segment 36–45 in NHR that weaken T20 binding [21], sometimes accompanied by secondary compensatory mutations in CHR that partially restore viral fitness [22]. Peptide inhibitors that interact with the NHR hydrophobic pocket show considerably improved inhibitory potency and increased genetic barrier to the appearance of resistance compared to T20 [11,12]. Additional residues upstream of the pocket-binding motif in the CHR sequence have also been recognized as critical for inhibition [23].

Class-2 inhibitors are typically engineered protein constructs that mimic exposed NHR grooves and target the pre-fusion intermediate by binding to the exposed CHR region. Different design approaches have been followed to stabilize the NHR helices in a trimeric coiled-coil conformation. These include covalent stabilization of the trimer by disulfide bridges and/or fusion of NHR segments to trimerization domains [24–26]. Also targeting the CHR region, a protein construct denoted 5-helix was engineered by connecting five out of the six helices that make up the core of the gp41 6HB structure using short peptide linkers [27]. Using a different approach, we previously designed single-chain small protein constructs by connecting with short loops two parallel NHR helices and an antiparallel one with the reverse sequence and stabilizing the trimeric bundle by engineering several mutations [28]. These small proteins, named covNHR, bind strongly to CHR-derived peptides and similarly to other class-2 constructs, potently inhibit various HIV-1 pseudoviruses and primary isolates at nanomolar concentrations. The covNHR proteins have several advantages over other constructs: namely, they can be produced by recombinant expression with high yield, are very soluble and structurally stable in physiological buffers and do not need any additional chemical modification.

Since class-2 inhibitors interfere with highly preserved interactions involving the hydrophobic pocket, they generally show a potent and broad inhibitory activity and very likely have a high genetic barrier for the development of resistance. On top of their interest as fusion inhibitors, engineered proteins displaying a fusion-intermediate-like, NHR groove have been used for the study of mechanism of HIV fusion. Many structural details about the modes of binding of antibodies, peptides and inhibitors have been obtained with these NHR constructs [29–31]. Highly relevant fine details about the HIV-1 fusion mechanism have been revealed by the use of 5-helix constructs as probes for fusion intermediate formation, accessibility and lifetime [32–34]. Moreover, NHR fusion intermediate mimics were used to select neutralizing antibodies that recognize the hydrophobic pocket [16,17], to elicit neutralizing sera by vaccination [35], and as targets in high-throughput screening assays to identify small molecule HIV-1 fusion inhibitors [14,36].

Despite this wealth of information, a full understanding of the determinants of the interaction between gp41 NHR and CHR is still incomplete. This is in part due to a lack of accurate thermodynamic data about the interaction using appropriate experimental models that may complement the abundant structural and functional information available. Here, we used the covNHR proteins as valuable model system for a fully exposed, complete NHR groove. A new covNHR protein was produced and compared with a previously described variant [28] that differs in two mutations, V10E and Q123R (equivalent to V38E and Q40R in the gp41 sequence), at the site of development of resistance to T20. A detailed calorimetric analysis allowed us to measure the thermodynamic contributions to the CHR–NHR interaction in each variant. The high-resolution structure of the complex between the new covNHR protein and the C34 peptide determined by x-ray crystallography provided fine structural details about the binding interactions and gave insight into the structural determinants of HIV-1 resistance to CHR peptides. In addition, the capacity of these covNHR proteins to inhibit a panel of HIV-1 pseudoviruses, including T20-resistant strains, was determined. The results improve our understanding of the mode by which the CHR region can be used as target to efficiently inhibit HIV-1 replication. These results will serve as guide for the improvement of strategies to block the early step of HIV-1 fusion.

Results

Design, production and characterization of covNHR variants

In our previous work [28], we designed and engineered several generations of single-chain covNHR proteins. In this engineering process, sets of mutations were introduced to stabilize the monomeric structure, minimize aggregation and

avoid unspecific binding to target CHR peptides. A final construct (formerly named covNHR3-ABC) contained mutations V10E and Q123R aimed to establish favorable electrostatic interactions between helices 1 and 3. These mutations are equivalent to V38E and Q40R in gp41 at the region of mutations that confer resistance to T20 treatment [21] (see also Discussion). Here, we produced a new covNHR variant by reversing these two mutations to WT amino acids. We refer in this work to each variant as covNHR-ER and covNHR-VQ according to the amino acids at positions 10 and 123, respectively (Fig. 1). The two variants were produced recombinantly by *Escherichia coli* expression with similarly high yields and are highly soluble at physiological pH.

Some experiments were carried out with variants containing an additional A154T mutation and a longer His-tag. For all purposes in this work, these Thr154 variants behaved identically to the Ala154 variants with respect to their stability and binding to CHR peptides.

The two covNHR proteins behave as monomeric according to DLS measurements in both pH 2.5 and pH 7.4 buffers [50 mM glycine/HCl (pH 2.5) and 50 mM sodium phosphate buffer (pH 7.4)], showing apparent hydrodynamic radii of 2.7–2.8 nm (Fig. S1a–b). Far-UV CD spectra indicate similar α-helical structures, with about 80–85% helix contents (Fig. 2a). Both proteins are very stable against thermal denaturation, with melting temperatures ranging between 90 °C at pH 2.5 and 105 °C at pH 7.4 (Fig. S1c–d). The covNHR-VQ variant was slightly more stable than covNHR-ER by 1–2 °C. In conclusion, the covNHR variants are monomeric, well folded and highly stable helical proteins and the two mutations at the site of T20 resistance do not affect significantly the structure, stability or oligomerization state.

Binding of CHR peptides

To characterize the interaction between the covNHR proteins and the CHR target region of gp41, we analyzed the binding of the C34 peptide (gp41 residues 117–150; Fig. 1) [1] to both covNHR variants. Far-UV CD spectroscopy shows an increase in α-helicity when the proteins and the peptide are mixed indicating acquisition of helical conformation by the peptide as a consequence of binding onto the NHR groove (Fig. 2a). The increase in negative ellipticity at 222 nm is significantly higher for covNHR-VQ than for covNHR-ER, suggesting a higher level of α-helical structure in the bound state. Near-UV CD spectra of the protein–peptide mixtures show a similar characteristic negative ellipticity band centered at 293 nm (Fig. 2b) that is associated with the stacking of CHR tryptophan side chains onto the hydrophobic pocket [37]. These spectra indicate a similar binding mode of C34 to both covNHR variants at the preserved pocket.

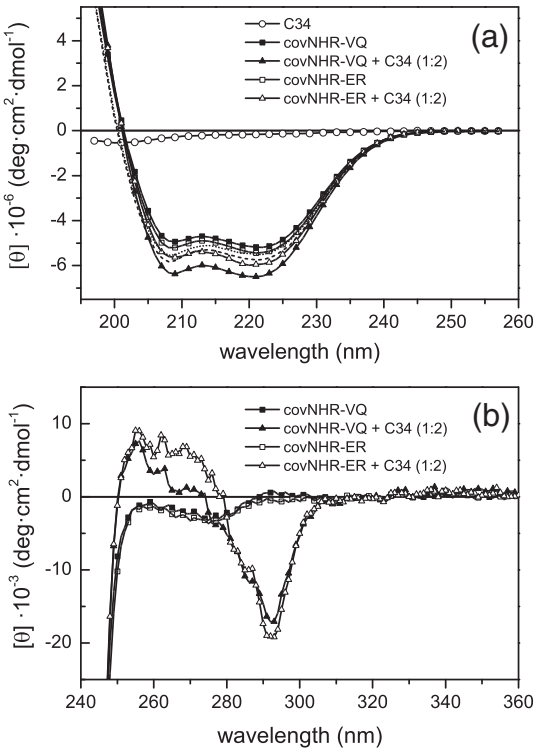

Fig. 2. Binding of C34 to covNHR proteins. Far-UV (a) and near-UV (b) CD spectra of free covNHR proteins and 1:2 mixtures of the proteins with C34 peptide. The CD signal is normalized as molar ellipticity units in both panels. The far-UV spectrum of C34 is also shown in circles, and the theoretical sum spectra of each protein and the peptide are represented in dotted and dashed lines for covNHR-VQ and covNHR-ER, respectively. The spectrum of C34 in panel b is almost flat and has been omitted for clarity. Protein concentrations used were 15 μM in panel a and 40 μM and in panel b.

To characterize the binding thermodynamics in detail, we performed ITC analysis by direct titration with C34 onto the protein solutions (Fig. 3a–b), with strikingly different results for the two variants. As previously reported [28], C34 binds to covNHR-ER with 1:1 stoichiometry and low nanomolar affinity (K_d = 14 ± 3 nM at 25 °C; see Table 1). The covNHR-VQ variant shows even higher affinity for C34. This affinity is so high that cannot be determined with accuracy by direct ITC titration. Also, the binding enthalpy of C34 to covNHR-VQ is more than 2-fold higher than to covNHR-ER indicating a much tighter interaction. Heat capacities of binding were determined by measuring the binding enthalpy at several temperatures for each variant (Fig. 3c). The binding heat capacity is significantly more negative for covNHR-VQ than for covNHR-ER (Table 1), consistently with a greater amount of surface occluded in the complex.

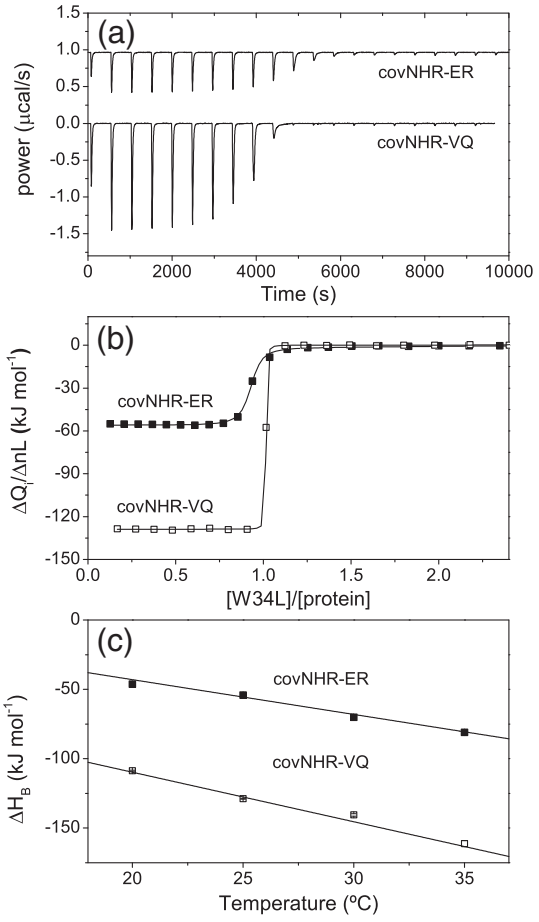

Fig. 3. Isothermal titration calorimetry of C34 binding to the covNHR proteins. (a) Experimental ITC thermograms measured by titration of 9.9 μM covNHR-ER with 220 μM C34 and 8.6 μM covNHR-VQ with 255 μM C34 at 25 °C. The thermograms have been corrected from the baseline and displaced vertically for the sake of clarity. (b) ITC binding isotherms calculated from the thermograms plotted in panel a. The symbols correspond to the experimental heats and the lines represent the fittings using a binding model of *n* identical and independent sites. (c) Temperature dependence of the experimental enthalpy of binding of C34 to the covNHR variants. The lines are the linear regressions to the experimental values that are plotted with symbols.

To attempt an accurate determination of the binding affinity between C34 and covNHR-VQ, we carried out DSC experiments with the free proteins and with protein–peptide mixtures at different molar ratios (Fig. 4). At pH 7.4, both free proteins undergo irreversible denaturation in the DSC scans showing asymmetric peaks at high temperatures (≈105 °C). The sharp drop on the high-temperature side of the peaks suggests thermally induced aggregation. In the presence of different amounts of peptide, the DSC peaks develop a prominent shoulder on the low-temperature side, as a result of endothermic peptide dissociation, which occurs partially decoupled to the unfolding of the proteins. The shoulder is much sharper and more pronounced for the covNHR-VQ:C34 mixtures, due to a higher enthalpy of dissociation. To analyze the DSC data and extract the binding constants, we used a Lumry–Eyring model for the irreversible denaturation of the protein, linked to a protein–peptide binding equilibrium. The mathematical development of the model and the analysis of the data are described in detail in the Supplemental Text S1 and Table S1. We globally fitted the DSC curves for each covNHR variant in the presence of different C34 concentrations. Binding enthalpies and heat capacity changes were fixed in the fittings using the values determined by ITC at 25 °C (Table 1). The resulting dissociation constants at 25 °C are 4.5 nM for covNHR-ER and 0.08 pM for covNHR-VQ. These results clearly indicate that the V10E and Q123R mutations strongly decrease binding strength by disrupting local interactions between the C-terminus of C34 and the site of T20 resistance in NHR.

To confirm this, we performed the ITC titration of covNHR-ER with T20. The data indicated very weak binding (Fig. S2a). Since the covNHR proteins do not contain the region complementary to the MPER residues of T20, we also titrated covNHR-ER with the Y24L peptide (gp41 residues 127–150) (Fig. 1b), which lacks the C-terminal MPER residues of T20. This peptide showed no detectable binding to covNHR-ER (Fig. S2a), confirming a direct local effect of the covNHR mutations and suggesting that the weak T20 binding may be unspecific and probably mediated by the hydrophobic MPER residues. In contrast, Y24L bound tightly to covNHR-VQ (Fig. S3b) with a K_d of 81 ± 15 nM and a considerably negative binding enthalpy (Table 1). T20 and covNHR-VQ co-aggregated strongly when mixed, precluding the corresponding ITC experiment. These results demonstrate that the ER mutations at the site of T20 resistance abolish the binding of T20 to the NHR region.

The thermodynamic magnitudes obtained from the calorimetric analysis are collected in Table 1 and summarized in Fig. 5. The extremely favorable binding enthalpy of C34 to covNHR-VQ is outstanding and results from a vast binding interface. The favorable enthalpy is only partially compensated by a considerable decrease in binding entropy, mainly due to the helical folding of the peptide upon binding. In contrast, the binding of C34 to covNHR-ER shows a smaller, albeit still favorable, binding enthalpy and relatively low binding entropy, consistent with a partially disordered peptide in the complex as a result of the ER mutations. Our calorimetric analysis demonstrates that the two mutations perturb the local interactions at the site of T20 resistance and result in a drastic reduction in affinity for covNHR-ER compared to covNHR-VQ.

Table 1. Thermodynamic parameters of binding of gp41 CHR peptides to covNHR proteins

Protein	Peptide	Temperature (°C)	K_b (M^{-1})	K_d (nM)	ΔH_b (kJ mol^{-1})	n	$\Delta C_{p,b}$ (kJ K^{-1} mol^{-1})
covNHR-VQ	C34	20	–	–	−108.6 ± 0.4	0.81	−3.6 ± 0.4
		25	–	–	−128.8 ± 0.3	1.01	
		30	–	–	−140.5 ± 0.9	0.93	
		35	–	–	−161.2 ± 2.2	0.88	
		25[a]	$(1.32 \pm 0.03) \times 10^{13}$	0.000076 ± 0.000002	−129[b]	1[c]	−3.6[b]
	T20	25	Not measurable due to co-aggregation				
	Y24L	25	$(1.2 \pm 0.2) \times 10^{7}$	81 ± 15	−68 ± 1	0.90	
covNHR-ER	C34	20	$(5.3 \pm 2.3) \times 10^{7}$	19 ± 8	−46.3 ± 0.4	0.94	−2.5 ± 0.4
		25	$(7.3 \pm 1.4) \times 10^{7}$	14 ± 3	−54.2 ± 0.2	0.95	
		30	$(2.8 \pm 0.6) \times 10^{7}$	35 ± 7	−70.2 ± 0.4	0.89	
		35	$(6 \pm 4) \times 10^{7}$	18 ± 13	−81 ± 1		
		25[a]	$(2.25 \pm 0.07) \times 10^{8}$	4.5 ± 0.2	−54.2[b]	1[c]	−2.5[b]
	T20	25	$(7 \pm 6) \times 10^{4}$	14,500 ± 13,400	−12 ± 6	1[c]	
	Y24L	25	Binding not detected				

Errors correspond to 95% confidence intervals of the fittings.
[a] Extrapolated to 25 °C from DSC analysis.
[b] Fixed in the fittings of the DSC data using the results from ITC at 25 °C.
[c] Fixed to 1 single binding site.

X-ray crystallography

The crystal structure of the covNHR-VQ protein in complex with C34 was determined at a resolution of 1.9 Å (Table S2, Fig. 6a). We were unable, however, to obtain crystals for the complex between covNHR-ER and C34, likely due to their lower affinity and partial structural disorder. The covNHR-VQ protein has a characteristic antiparallel trimeric coiled-coil, as previously described for the free covNHR-ER protein (PDB entry 4R61) [28]. The backbone RMSD between the two proteins is 0.77 Å for the commonly visible residues (Fig. 6b). However, inter-helix distances are slightly reduced in the covNHR-VQ:C34 complex compared to free covNHR-ER by an average of 0.56 Å, suggesting tighter internal packing in the NHR coiled-coil, presumably due to peptide binding and complex formation. Also, the second loop in covNHR-VQ is well resolved in the structure of the complex, whereas in free covNHR-ER, this loop is not visible in the electron density map. This indicates a lower conformational flexibility in the covNHR-VQ:C34 complex due to the stabilizing protein–peptide interactions.

Structural alignment of the complex structure with other gp41-based constructs representing the post-fusion 6HB structure shows a striking homology, both in the backbone conformation and in the protein–peptide interactions (Fig. 6c). The pocket-binding motif shows a very similar insertion of Trp–Trp–Ile side chains into the hydrophobic pocket, and most contacts along the remaining binding interface are virtually identical. Interestingly, several buried water molecules could be defined in the structure (Fig. 7). One of these buried waters occupies a cavity in the center of the NHR antiparallel coiled-coil. More importantly, the protein–peptide interface also contains four well-defined buried waters exposing less than 10 $Å^2$ of surface area (Table S3). A fully buried water molecule fills an interfacial cavity lined by the side chains of Val10, Gln13, Ile120 and Gln123 from covNHR-VQ, and Gln26 and Asn29 from C34 (Fig. 7a). This water molecule bridges side chains from the three different helices by hydrogen bonds and van der Waals contacts. Disruption of these water-mediated interactions by the V10E and Q123R mutations in the covNHR-ER variant explains the strong local impairment of binding affinity. Another partially buried water occupies a cavity created by the absence of side chain of Gly119, which is structurally equivalent to Gly36 in gp41 (Fig. 7b). Two additional interfacial waters bridge laterally the NHR and CHR regions (see Table S3). All residues interacting with these buried waters are highly preserved, suggesting a crucial role of these water-mediated interactions in HIV-1 fusion. Structurally homologous water molecules can also be observed in a number of gp41 constructs representing post-fusion structures or in NHR–CHR peptide complexes (Table S3).

The crystallographic structure of the covNHR-VQ:C34 complex demonstrates that the covNHR proteins are excellent mimetic molecules of a fully exposed NHR groove and reproduce very accurately the NHR–CHR interactions found in trimeric gp41.

Structure-based calculation of thermodynamic magnitudes

Using the three-dimensional structure of the covNHR-VQ:C34 complex, we estimated the enthalpy and heat capacity of binding based on the changes of solvent-accessible surface area (SASA). As described in Materials and Methods, the calculation

has been split in two terms: the folding of the C34 peptide, which is disordered in its free form, into its bound helical conformation, and a rigid-body binding between the peptide and the protein including burial of interfacial water molecules. The results of the calculation are summarized in Table S4 in the Supplementary Material. The folding of the peptide to its α-helical bound conformation buries a considerable amount of SASA, in majority polar, resulting in a strongly negative enthalpy contribution and a small contribution to the heat capacity change. In contrast, the binding process involves mainly burial of apolar SASA, and therefore, its contribution to the binding enthalpy is small and positive but it explains most of the negative binding heat capacity change. Burial of four interfacial water molecules also makes a strong contribution to the negative binding enthalpy, which is crucial for the exothermic signature of the global process. The calculated global ΔH_b and $\Delta C_{p,b}$ values (–97 kJ mol^{-1} and –2.8 kJ K^{-1} mol^{-1}, respectively) have the same signature but are significantly smaller in magnitude than those measured experimentally (–129 kJ mol^{-1} and –3.6 kJ K^{-1} mol^{-1}). These differences may be attributed to a conformational tightening of covNHR-VQ upon binding. Buffer protonation due to proton exchange with binding can be neglected for the purpose of this comparison because the ITC experiments have been made in phosphate buffer, which has a small heat of ionization at pH 7.4.

HIV-1 neutralization

The structural and thermodynamic characterization shown above reveals drastic differences in affinity between the covNHR proteins and their CHR target due to the local perturbation at the NHR–CHR interface produced by the V10E and Q123R mutations. This prompted us to explore the influence of these mutations upon the capacity of the covNHR proteins to inhibit HIV-1 infection. The inhibitory activity of covNHR-ER and covNHR-VQ was analyzed using the conventional TZM-bl assay and compared to that of T20 and C34. We observed that both covNHR variants potently inhibit replication of a panel of HIV-1 pseudoviruses of different clades [38] (Table 2). The inhibitory potency of covNHR-ER is lower than that of covNHR-VQ with slightly but consistently higher IC50 values for all viruses tested. These results are in accordance with the perturbation of the binding to the CHR target produced by the ER mutations, although the small decrease in inhibitory potency is not in correspondence with the huge difference in affinity for C34 measured in the binding experiments. Moreover, the IC50 values of covNHR-VQ are of similar low nanomolar magnitude as those measured for C34 for all viruses except for the CN54 virus. This primary virus was slightly (about 10-fold) less efficiently inhibited by the covNHR proteins. T20 was very effective in inhibiting some HIV-1

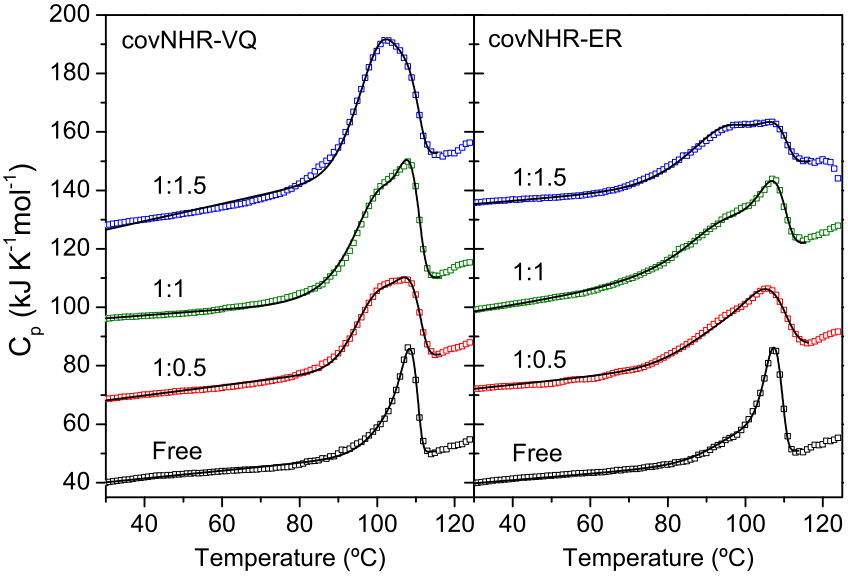

Fig. 4. DSC analysis of the thermally induced unfolding of covNHR:C34 complexes. The DSC thermograms were recorded at a scan rate of 2 °C min^{-1} for each covNHR variant at a concentration of 40 μM in the absence (free) and in the presence of C34 at several molar ratios as indicated along each curve. The DSC thermograms were corrected from the buffer baseline and from the influence of the heat capacity of the free ligand. Symbols represent the experimental data. The black solid lines correspond to the global fitting carried out using a Lumry–Eyring denaturation model linked to ligand binding. The details of this analysis are described in the Supplementary Text S1. The thermograms have been displaced along the *y*-axis by 30 kJ K^{-1} mol^{-1} intervals for the sake of clarity.

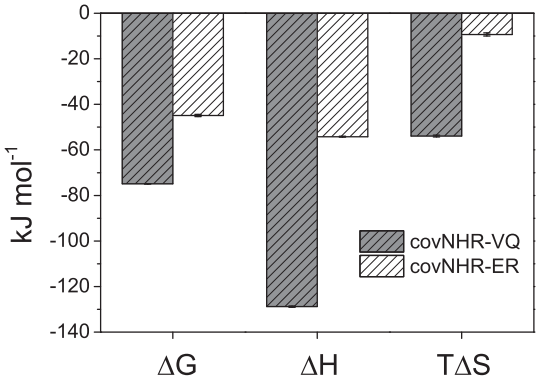

Fig. 5. Thermodynamic parameters of C34 binding to covNHR proteins. The values have been obtained from Table 1.

strains, but its activity was considerably reduced for other strains such as TRO11, 398F1 and SF162 (Table 2).

To explore the influence of mutations at the site of T20 resistance, we assayed the inhibitory activity of covNHR proteins on the replication of a T20-resistant pNL4-3 DIM mutant (Fig. 8). The pNL4-3 virus has an Asp36 residue in place of Gly at the GIV motif of NHR, and the T20-resistant DIM variant has additionally Met38 in place of Val. Both covNHR-ER and covNHR-VQ inhibited very efficiently WT and DIM pNL4-3 with low nM IC50 and showed no sensitivity to the V38M mutation in gp41. In contrast, the inhibitory activity of C34 and especially of T20 was reduced by the mutations at the site of resistance. These results clearly demonstrate a broad inhibitory potency of the covNHR proteins to primary HIV-1 strains of various origins. Moreover, the covNHR proteins were able to inhibit T20-resistant strains demonstrating their insensitivity to escape mutations for CHR-based inhibitors.

Discussion

Structural and thermodynamic features of the NHR–CHR interaction

This work highlights the potential of the covNHR protein constructs as extremely accurate mimics of an exposed NHR surface and shows that these proteins constitute useful models to investigate the gp41 interactions that drive HIV-1 fusion. Our high-resolution structure of the complex between covNHR-VQ and the C34 peptide shows NHR–CHR interactions virtually identical to those reported for the post-fusion structure of gp41, including preserved buried water molecules at the binding interface. Together with this structural information, the thermodynamic magnitudes derived from our calorimetric analysis provide significant insight into the forces that drive HIV-1 fusion, inhibition by peptides and acquisition of resistance.

We have found extremely high binding affinity of covNHR-VQ for C34 (gp41 residues 117–150) ($K_d \approx 0.08$ pM), among the highest binding affinities reported for CHR–NHR interactions in gp41-based constructs. Comparable dissociation constant of 0.6 pM was reported by fluorimetric methods for the interaction between 5-helix, also exposing a stabilized NHR surface, and C37 (gp41 residues 625–661) [32]. However, detailed calorimetric studies of extensive CHR–NHR interactions are very scarce, probably due to the lack of well-behaved gp41 constructs. Most studies report limited titration experiments directed to evaluate binding affinities of mutated constructs or modified peptides. For instance, He *et al.* [39] reported ITC measurements of binding between C34 and several N36 mutants, with affinities in the high nanomolar or micromolar range, although aggregation of N36 produced anomalous stoichiometry. Similar affinities were obtained for binding of N36 and N46 to C34 mutants [40]. ITC experiments with gp41 constructs stabilizing an exposed NHR are also scarce. For instance, Deng *et al.* [41] measured the binding of CHR peptides to 5-helix, reporting relatively low affinities in the mid-to-high nanomolar range ($K_d = 0.8$ μM for C34), in contrast with the sub-picomolar values reported here and by Root and coworkers [32]. More detailed thermodynamic studies have been reported using IQN17, another NHR mimic, but only limited to binding of short CHR peptides (D-peptides, cyclic peptides and helically constrained short peptides) targeting the hydrophobic pocket [30,42]. In all cases, these short peptides showed micromolar or lower affinities, suggesting that strong CHR–NHR binding affinity results from a large interaction interface.

The extremely high affinity and large negative binding Gibbs energy of C34 to covNHR-VQ are the result of a strong compensation between a very large favorable enthalpy partially opposed by a large unfavorable entropy, typical of extensive protein–protein interactions. Also, the negative heat capacity of binding is the result of burial of a large SASA as determined from the structure of the complex. Prediction of the binding enthalpy and heat capacity on the basis of burial of polar and apolar SASA using a model of binding to a rigid covNHR protein does not explain, however, the large magnitude of the experimental values, suggesting considerable contribution from structural tightening of internal contacts in the NHR coiled-coil produced by binding. This tightening is evidenced by a small but significant decrease in interhelical distances observed between covNHR-VQ in complex with C34 and the free covNHR-ER protein [28].

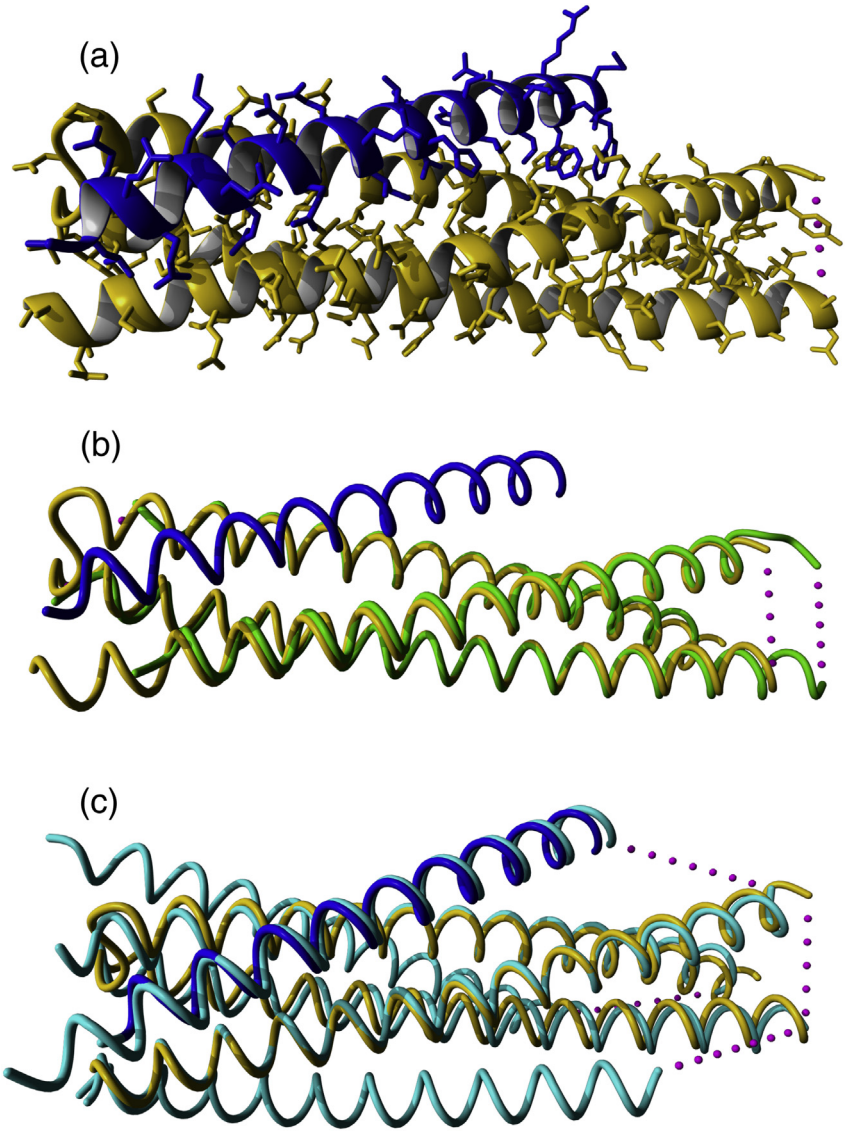

Fig. 6. Crystallographic structure of covNHR-VQ in complex with C34. (a) Overall complex structure. CovNHR-VQ is in golden color and the C34 peptide in blue. The backbone is represented in ribbons and the side chains with sticks. (b) Structural backbone alignment between covNHR-VQ (golden) and covNHR-ER (green) (PDB code 4r61) [28]. The C34 peptide in the complex is colored in blue. (c) Structural backbone alignment between the covNHR-VQ:C34 complex (golden and blue) and a chimeric gp41-based construct representing the post-fusion 6-helix-bundle conformation (cyan) (PDB code 1env) [8]. The GCN4 region that stabilizes this construct is hidden for the sake of clarity. Dots indicate missing or unresolved chain segments in all panels.

Molecular mechanism of resistance to CHR-peptide inhibitors

Long-term treatment with enfuvirtide progressively develops HIV-1 variants with single, double or multiple mutations at residues 36 to 45 of NHR [22,43]. Mutations at Val38 are particularly frequent and primarily occur to amino acids with smaller (Ala, Gly, Ser) or larger (Met, Trp) side chains perturbing van der Walls contacts at the site [44]. In addition, mutation V38E confers particularly high resistance to T20 [43] and can also cause resistance to C34 [45] and to the second-generation inhibitor T-1249 [44]. Mutations at Gln40 also arise in response to T20 treatment, generally to positively charged aminoacids [46]. It is highly plausible that other single or multiple mutations at this locus would produce similar perturbations to those described here for the ER mutations.

Our structural and thermodynamic analysis provides a clear molecular interpretation for the acquisition of resistance against CHR-derived peptide inhibitors. As a result of the ER mutations, the binding affinity for C34 is reduced in covNHR-ER by 5 orders of magnitude compared to covNHR-VQ (the binding Gibbs energy increases by about

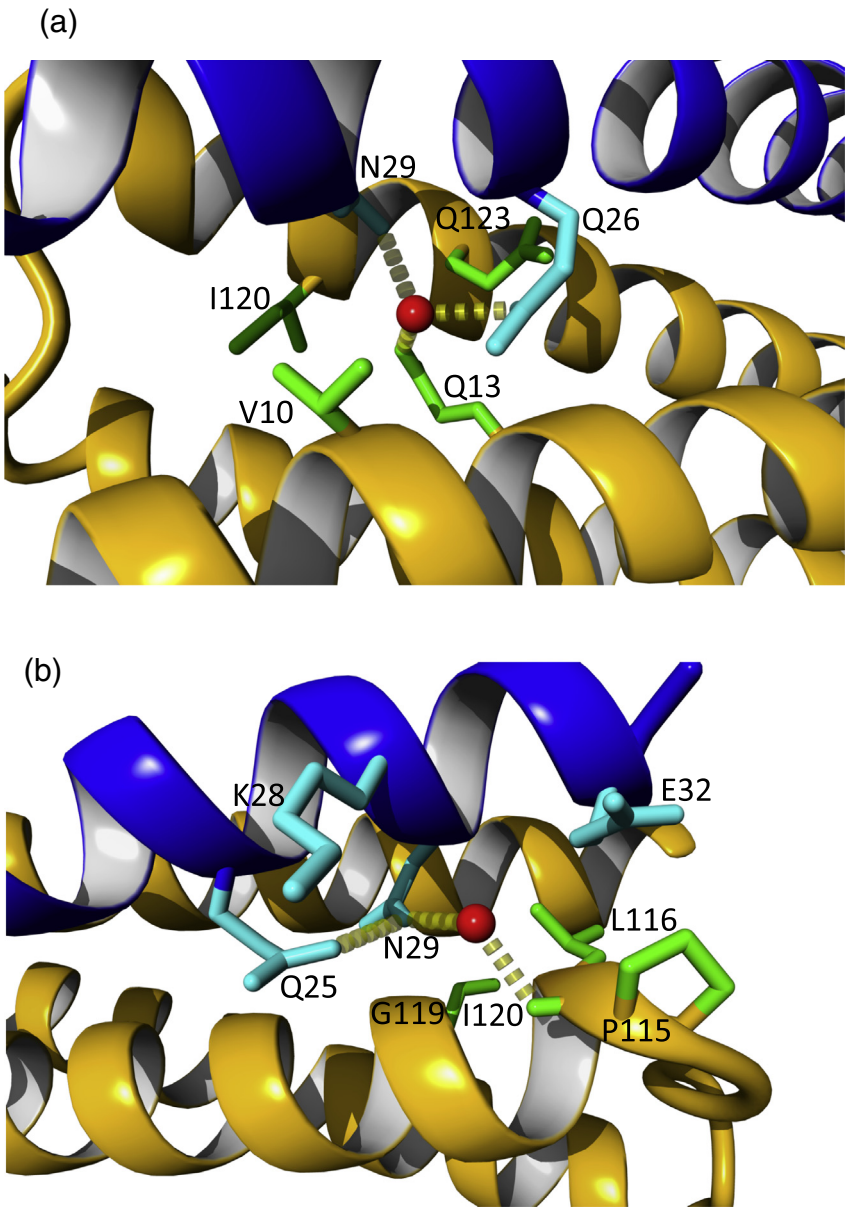

Fig. 7. Interfacial water molecules in the covNHR-VQ:C34 complex. Buried water molecules HOH308A (a) and HOH310A (b) at the CHR–NHR binding interface in the covNHR-VQ:C34 complex. Residues lining the cavities occupied by the water molecules are labeled and their side chains represented in sticks. Blue and cyan colors correspond to C34 and green and golden colors to covNHR-VQ. Yellow dotted lines indicate hydrogen bonds.

30 kJ mol^{-1}). This is mainly the result of a strong increase in binding enthalpy, opposed by an increase in the entropic term. The observed change in the negative heat capacity of binding is consistent with a reduced binding interface (by about one third) as a result of the local impairment of interactions. These changes in thermodynamic parameters indicate that the ER mutations, structurally equivalent to V38E and Q40R in gp41, completely disrupt local interactions at the site of resistance to T20. Any replacement of Glu for Val10 or Arg for Gln123 would fill the cavity occupied by a buried water molecule perturbing a clear interaction network (Fig. 7a). Similarly strong affinity decreases for C37 have been reported for V38D or V38E 5-helix mutants [32], suggesting that the V38E single mutation suffices to completely disrupt binding at the T20-resistance motif. Interestingly, another partially buried water (Fig 7b), also preserved in other post-fusion gp41 structures, would also be structurally displaced by the side chains of Asp36 or Ser36 frequently found for T20-resistant viruses [21]. This local perturbation explains the low

Table 2. *In vitro* HIV-1 inhibition by covNHR proteins and CHR peptides

Pseudovirus	Clade	covNHR-ER	covNHR-VQ	T20	C34
BG505	A	34 ± 1	13 ± 1	4 ± 0.4	4 ± 2
TRO11	B	46 ± 3	16 ± 4	38 ± 4	16 ± 4
25,710	C	25 ± 1	12 ± 1	4 ± 3	3 ± 0.4
398F1	A	65 ± 3	11 ± 3	147 ± 10	14 ± 1
CE1176	C	30 ± 3	13 ± 0.3	4 ± 2	10 ± 1
CN54[a]	B′/C	96 ± 22	43 ± 10	2 ± 1	8 ± 2
SF162	B	33 ± 5	8 ± 2	51 ± 1	10 ± 1
MW965.26	C	9 ± 2	2 ± 1	4 ± 1	1 ± 0.1
pNL4-3	B	5.1 ± 0.3	2.0 ± 0.4	38 ± 3	3.1 ± 0.3
pNL4-3(DIM)[b]	B	6 ± 1	3.1 ± 0.3	494 ± 256	15 ± 1

Inhibitory activity (IC50 in nM ± S.D. of triplicates) was measured with the standard TZM-bl assay using pseudoviruses with Env of several clades, a primary virus and a T20-resistant strain.
[a] Primary isolate.
[b] T20-resistant strain.

inhibitory potency of T20 for pNL4.3 viruses, which have Asp instead of Gly36. The role of water molecules participating in the binding interfaces has been reported to profoundly influence binding thermodynamics, strongly contributing to the negative binding enthalpy [47,48]. Our results clearly show how these water-mediated interactions can play a role on the mechanisms of acquisition of resistance and support that the covNHR proteins use their highly preserved, hydrophobic pocket to target the pocket-binding motif in CHR and block fusion.

CovNHR proteins as potent and broad HIV-1 inhibitors

Since pocket mediated interactions are highly preserved and essential for infection, the covNHR binding properties should confer them a broad activity against numerous strains with distinct CHR sequences and therefore with likely high genetic barrier to resistance acquisition. Indeed, we found that covNHR-VQ and covNHR-ER display a broad inhibitory potential against a panel of viruses representing wide genetic variabilities [38]. An alignment of gp41 sequences of the viruses tested in this work (Table S5), compared to our reference sequence, shows that the whole NHR region is highly preserved, whereas the CHR region shows higher variability, especially at its mid region.

Despite the strong decrease in affinity for CHR produced by the ER mutations at the site of T20-resistance, covNHR-ER still maintains strong inhibitory potency for a wide variety of viruses of different clades. Compared to the covNHR-VQ variant, the inhibitory potency is decreased by only 2- to 5-fold, implying that local interactions at the T20-resistance motif are not required for effective blockage of HIV-1 fusion by targeting CHR and can be weakened or even abolished without a dramatic effect in inhibitory potency. Likewise, T20-resistant viruses, with the same local CHR–NHR interactions weakened or disrupted, maintain significant infectivity [44], which suggest that membrane fusion does not require a complete, tight NHR–CHR interaction involving the T20 binding site.

As discussed above, T20 and other CHR peptidomimetics, even those containing the pocket-binding motif, are susceptible to the appearance of resistant viruses. The single V38E mutation elicits 100-fold resistance to C37 inhibition in HXB2 pseudoviruses [34] and 24-fold resistance to T-1249 in LAI viruses [44]. Therefore, impairment of local interactions at the site of resistance has asymmetric effects for class-1 and class-2 inhibition. This supports a different mechanism of gp41 inactivation by each type of inhibitor and an asymmetric exposure of CHR and NHR during the fusion cascade [33]. Recent work has shown that the transition from native to fusion-activated Env involves several states and pathways that depend on CD4 density and on correceptor participation, with progressive and asymmetric exposure of NHR and CHR regions [49,50]. In this regard, the remarkable (exceptional) binding affinity of covNHR-VQ may be extremely useful. Moreover, the very tight interactions of covNHR-VQ with CHR and its capacity to target highly preserved motifs may limit the appearance of HIV-1 escape variants. Whether covNHR-VQ would prevent or limit the generation of HIV-1 resistance escape mutants needs to be further investigated.

In conclusion, the covNHR proteins are highly stable and very accurate mimics of an exposed NHR coiled-coil, providing a very useful model to investigate fine details of the molecular determinants of fusion inhibition targeting gp41. Moreover, their broad inhibitory activity, together with amenable biophysical properties, makes these covNHR proteins particularly attractive as fusion inhibitors compared to NHR-targeting inhibitors. Our results could help in the development of new strategies of HIV-1 inhibition based on gp41 NHR mimetics in a pre-fusion conformation.

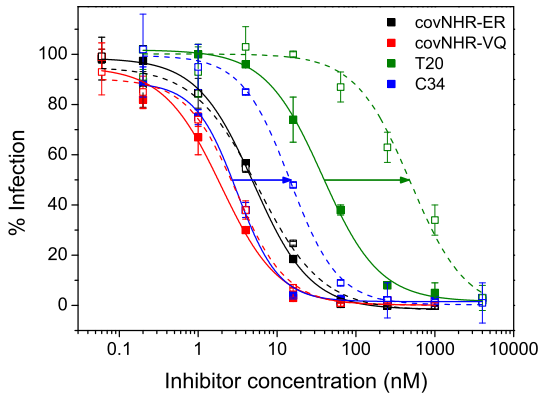

Fig. 8. Effect of T20 resistance on the HIV-1 inhibitory activity of covNHR proteins. *In vitro* inhibition of WT pNL4-3 (solid symbols) and V38M mutant pNL4-3 (open symbols) pseudoviruses infection of TZM-bL cells by fusion inhibitors added at different concentrations. Data are the mean ± S.D. of three independent measurements. Regression curves of WT pNL4-3 (solid lines) and V38M mutant of pNL4.3 (dashed lines) are plotted. Arrows indicate the shifts in IC50 observed for T20 and C34 (see Table 2).

Materials and Methods

Protein and peptide samples

The NHR and CHR gp41 sequences used in this work are described in Fig. 1. The reference gp41 sequence was taken from the full gp160 precursor glycoprotein of the HIV-1 BRU isolate (Swiss-Prot entry sp.|P03377|ENV_HV1BR). The covNHR proteins were produced by overexpression in *E. coli*, as described previously [28]. Synthetic CHR peptides, both N-acetylated and C-amidated, were acquired from Genecust (Luxembourg), with a purity >95%. Protein and peptide concentrations were determined by UV absorption measurements with extinction coefficients calculated according to their respective amino acid sequences with the ExPasy ProtParam server (https://web.expasy.org/protparam/) [51].

Circular dichroism

CD spectra were recorded in a Jasco J-715 spectropolarimeter (Jasco, Tokyo, Japan) equipped with Peltier-thermostatic cell holder. Measurements of the far-UV CD spectra (260–200 nm) were made with a 1-mm path length quartz cuvette at a protein concentration of ~15 μM. Spectra were recorded at a scan rate of 100 nm/min, 1-nm step resolution, 1-s response, and 1-nm bandwidth. The resulting spectra were usually the average of five scans. Near-UV CD spectra (350–250 nm) were measured at a protein concentration of ~40 μM using a 5-mm cuvette and were typically the average of 20 scans. Each spectrum was corrected by baseline subtraction using the blank spectrum obtained with the buffer, and finally, the CD signal was normalized as ellipticity units per mole of protein ([θ], in deg. $dmol^{-1}$ cm^2). The percentage of α-helical structure was estimated from the far-UV CD spectra as described elsewhere [52].

Dynamic light scattering

The particle sizes of the covNHR proteins were assessed by DLS measurements using a DynaPro MS-X instrument (Wyatt, Santa Barbara, CA). Dynamics software (Wyatt Technology Corporation, Santa Barbara, CA, USA) was used in data collection and processing. Sets of DLS data were measured at 25 °C with an average number of 50 acquisitions and an acquisition time of 10 s.

Isothermal titration calorimetry

ITC measurements were carried out in a Microcal VP-ITC calorimeter (Malvern Instruments, Worcestershire, UK). The protein solutions were titrated with 25 injections of the peptide solution using a profile of variable injection volumes, at 480-s intervals. Concentrations of the protein used for the titrations were in the range of 10–20 μM, while the ligands in the syringe were typically at 200–300 μM. The experiments were carried out in 50 mM phosphate buffer (pH 7.4) at 25 °C unless specifically stated. As a blank, an independent experiment with only buffer in the calorimeter's cell was performed with the same peptide solution to determine the corresponding heats of dilution. The experimental thermograms were baseline corrected, and the peaks were integrated to determine the heats produced by each ligand injection. Finally, each heat was normalized per mole of added ligand. The resulting binding isotherms were fitted using a binding model of independent sites, allowing the determination of the binding constant, K_b, the binding enthalpy, ΔH_b, and the binding stoichiometry, n, for each interaction. From these values, the Gibbs energy and entropy of binding could be derived as $\Delta G_b = -RT \cdot \ln K_b$ and $T \cdot \Delta S_b = \Delta H_b - \Delta G_b$.

Differential scanning calorimetry

Thermal unfolding experiments of the covNHR proteins were carried out in a Microcal VP-DSC microcalorimeter equipped with autosampler (Malvern Instruments, Worcestershire, UK). Scans were run from 5 to 125 °C at a scan rate of 120 °C h^{-1}. Protein concentration was typically 40 μM. Baselines recorded with buffer in both cells were obtained before each experiment and subtracted from the experimental thermograms obtained with the protein samples.

Reheating runs were carried out to determine the thermal reversibility of the thermal denaturation, with the exact same parameters used for the main scan. After correction of the dynamic response of the instrument, the partial molar heat capacity (C_p) was calculated from the experimental DSC thermograms using Origin 7.0 (OriginLab, Northampton, MA). Reversible unfolding thermograms were fitted using the two-state unfolding model, N ↔ U. In case of irreversible unfolding, we used a simple Lumry–Eyring denaturation model (N ↔ U → F) to fit the experimental thermograms [53]. To analyze the DSC thermograms measured with mixtures of covNHR proteins and peptides, we employed a 1:1 binding model (N + L ↔ NL) coupled to the Lumry–Eyring model. All equations used to fit the DSC data are described in the Supplemental Data (Supplemental Text S1) and were implemented in Origin software (Originlab, Northampton, MA).

Protein crystallization

Screening for initial crystallization conditions was performed by the sitting-drop vapor-diffusion method using commercially available crystal screening kits Proplex and Structure Screen 1 and 2 from Molecular Dimensions (Suffolk, UK). The covNHR-VQ-C34 complex solution (protein:peptide ratio 1:2) was prepared in 10 mM Tris and 0.05% NaN_3 (pH 7.5) 1 day before the experiment. Droplets consisting of 2 μL complex solution and 2 μL reservoir solution were equilibrated at 298 K against 200 μL reservoir solution in 48-well MRC Maxi Optimization plates (Cambridge, UK). Several favorable conditions were initially identified and were optimized to obtain crystals. The best diffracting crystals were obtained in 20% PEG 4 K and 0.1 M Mes (pH 6.5) using the sitting-drop setup using 10 μL drops 1:1 mixture of the covNHR-VQ:C34 complex at 12 $mg \cdot mL^{-1}$ in 10 mM Tris, pH 7.5 and equilibrated against 200 μL.

X-ray diffraction data collection, structure solution and refinement

For data collection, crystals were flash-cooled in liquid nitrogen. Data sets were collected at 100 K at the beamline ID30B at the ESRF (Grenoble, France) [54]. Diffraction data were indexed and integrated with the AutoPROC toolbox [55]. Data scaling was performed using the program Aimless [56] from the CCP4 suite [57]. Data collection statistics are collected in Table S2. Solution and refinement of the structures were performed using the PHENIX suite [58]. Molecular-replacement phasing using PHASER [59] was performed with the coordinates of the crystallographic structure of the covNHR3-ABC (PDB entry 4R61) [28]. Manual model building was performed using COOT [60,61]. Refinement was performed using phenix.refine in PHENIX [62]. Quality of the structures was checked using MOLPROBITY [63] and PROCHECK [64]. Structural refinement statistics are collected in Table S2. The complex coordinates were deposited at the Protein Data Bank under the accession code 62RG.

Structure-based thermodynamic calculations

The enthalpy and heat capacity changes of C34 binding to covNHR-VQ were estimated from the changes in SASAs. We divided the calculation in two processes: (1) folding of the C34 peptide from a disordered conformation to the bound helical structure and (2) rigid-body binding between the folded peptide and the protein. Conformational changes in the protein due to binding were neglected in this calculation. The SASA values of the disordered C34 peptide were estimated as described elsewhere [65]. The SASA values of the protein, the peptide and the complex were calculated with the coordinates of x-ray structure of the covNHR-VQ:C34 complex using the Lee and Richards algorithm [66] with default parameters for the water probe radius (1.4 Å), *z*-slice (0.25 Å). Averaged SASA values were obtained from 64 different orientations of the molecules with respect to the slicing plane. Buried water molecules exposing less than 10 $Å^2$ at the binding interface were considered in the bound state as part of the complex structure (see Results) and in the unbound state with the SASA of a fully exposed water molecule (98.5 $Å^2$). SASA changes were used to estimate the binding enthalpy and heat capacity using empirical parameters described elsewhere [67,68].

HIV-1 neutralization assays

The inhibition of HIV replication was determined using the conventional TZM-bl assay measured as a function of reductions in Tat-regulated Firefly luciferase (Luc) reporter gene expression [69]. The viruses used for TZM-bl cell infection were either WT HIV pNL4.3 strain or the DIM mutated T20-resistant strain [70]. Moreover, a panel of pseudoviruses expressing Env from primary isolates from several subtypes [38] was tested for HIV inhibitory potential. The IC50, the concentration (in nM) of inhibitor inducing a 50% decrease in relative luminometer units (RLU), corresponding to a 50% decrease in virus replication was calculated by non-linear regression using a sigmoidal Hill function, as implemented in Origin software (Originlab, Northampton, MA).

Accession numbers

PDB ID: 62RG.

Acknowledgments

We thank Dr. I. Luque for her help and advice in the SASA calculations and the estimation of the binding thermodynamic parameters. S. Jurado acknowledges a short-term fellowship from Boehringer-Ingelheim Fonds. M. Cano-Muñoz is hired by a contract from the Program for Warranty of Young Employment of the European Social Fund. This work has been funded by grants BIO2016-76640-R and BIO2016-78020-R from the Ministry of Economy and Competitiveness, Spain, and by the European Fund for Regional Development from the European Union. This work was also supported by ANRS and the Vaccine Research Institute for the Investissements d'Avenir program managed by the ANR under reference ANR-10-LABX-77 to C.M. X-ray diffraction data collection was supported by ESRF (Grenoble, France; BAG MX1938-beamline ID30B) and ALBA (Barcelona, Spain; BAG 2017082320-beamline Xaloc).

Appendix A. Supplementary data

Supplementary data to this article can be found online at https://doi.org/10.1016/j.jmb.2019.06.022.

Received 12 April 2019;
Received in revised form 21 June 2019;
Accepted 21 June 2019
Available online 27 June 2019

Keywords:
envelope glycoprotein;
fusion inhibitor;
calorimetry;
binding;
x-ray crystallography

Abbreviations used:
Env, HIV-1 envelope glycoprotein; gp41, glycoprotein subunit 41; gp120, glycoprotein subunit 120; CD, circular dichroism spectroscopy; ITC, isothermal titration calorimetry; DLS, dynamic light scattering; DSC, differential scanning calorimetry; SASA, solvent accessible surface area.

References

[1] D.C. Chan, P.S. Kim, HIV entry and its inhibition, Cell 93 (1998) 681–684.
[2] D.M. Eckert, P.S. Kim, Mechanisms of viral membrane fusion and its inhibition, Annu. Rev. Biochem. 70 (2001) 777–810.
[3] T.A. White, A. Bartesaghi, M.J. Borgnia, J.R. Meyerson, M.J. de la Cruz, J.W. Bess, R. Nandwani, J.A. Hoxie, J.D. Lifson, J.L. Milne, S. Subramaniam, Molecular architectures of trimeric SIV and HIV-1 envelope glycoproteins on intact viruses: strain-dependent variation in quaternary structure, PLoS Pathog. 6 (2010), e1001249.
[4] A.B. Ward, I.A. Wilson, The HIV-1 envelope glycoprotein structure: nailing down a moving target, Immunol. Rev. 275 (2017) 21–32.
[5] J.B. Munro, W. Mothes, Structure and dynamics of the native HIV-1 Env trimer, J. Virol. 89 (2015) 5752–5755.
[6] G.B. Melikyan, Membrane fusion mediated by human immunodeficiency virus envelope glycoprotein, Curr. Top. Membr. 68 (2011) 81–106.
[7] D.C. Chan, D. Fass, J.M. Berger, P.S. Kim, Core structure of gp41 from the HIV envelope glycoprotein, Cell 89 (1997) 263–273.
[8] W. Weissenhorn, A. Dessen, S.C. Harrison, J.J. Skehel, D.C. Wiley, Atomic structure of the ectodomain from HIV-1 gp41, Nature 387 (1997) 426–430.
[9] H.A. Yi, B.C. Fochtman, R.C. Rizzo, A. Jacobs, Inhibition of HIV entry by targeting the envelope transmembrane subunit gp41, Curr. HIV Res. 14 (2016) 283–294.
[10] J.M. Kilby, S. Hopkins, T.M. Venetta, B. DiMassimo, G.A. Cloud, J.Y. Lee, L. Alldredge, E. Hunter, D. Lambert, D. Bolognesi, T. Matthews, M.R. Johnson, M.A. Nowak, G.M. Shaw, M.S. Saag, Potent suppression of HIV-1 replication in humans by T-20, a peptide inhibitor of gp41-mediated virus entry, Nat. Med. 4 (1998) 1302–1307.
[11] J.J. Eron, R.M. Gulick, J.A. Bartlett, T. Merigan, R. Arduino, J.M. Kilby, B. Yangco, A. Diers, C. Drobnes, R. DeMasi, M. Greenberg, T. Melby, C. Raskino, P. Rusnak, Y. Zhang, R. Spence, G.D. Miralles, Short-term safety and antiretroviral activity of T-1249, a second-generation fusion inhibitor of HIV, J. Infect. Dis. 189 (2004) 1075–1083.
[12] Y. He, Y. Xiao, H. Song, Q. Liang, D. Ju, X. Chen, H. Lu, W. Jing, S. Jiang, L. Zhang, Design and evaluation of sifuvirtide, a novel HIV-1 fusion inhibitor, J. Biol. Chem. 283 (2008) 11126–11134.
[13] B.D. Welch, A.P. VanDemark, A. Heroux, C.P. Hill, M.S. Kay, Potent D-peptide inhibitors of HIV-1 entry, Proc. Natl. Acad. Sci. U. S. A. 104 (2007) 16828–16833.
[14] G. Frey, S. Rits-Volloch, X.-Q. Zhang, R.T. Schooley, B. Chen, S.C. Harrison, Small molecules that bind the inner core of gp41 and inhibit HIV envelope-mediated fusion, Proc. Natl. Acad. Sci. U. S. A. 103 (2006) 13938–13943.
[15] L. Lu, F. Yu, L. Cai, A.K. Debnath, S. Jiang, Development of small-molecule HIV entry inhibitors specifically targeting gp120 or gp41, Curr. Top. Med. Chem. 16 (2016) 1074–1090.
[16] M.D. Miller, R. Geleziunas, E. Bianchi, S. Lennard, R. Hrin, H. Zhang, M. Lu, Z. An, P. Ingallinella, M. Finotto, M. Mattu, A.C. Finnefrock, D. Bramhill, J. Cook, D.M. Eckert, R. Hampton, M. Patel, S. Jarantow, J. Joyce, G. Ciliberto, R. Cortese, P. Lu, W. Strohl, W. Schleif, M. McElhaugh, S. Lane, C. Lloyd, D. Lowe, J. Osbourn, T. Vaughan, E. Emini, G. Barbato, P.S. Kim, D.J. Hazuda, J.W. Shiver, A. Pessi, A human monoclonal antibody neutralizes diverse HIV-1 isolates by binding a critical gp41 epitope, Proc. Natl. Acad. Sci. U. S. A. 102 (2005) 14759–14764.
[17] D. Corti, J.P. Langedijk, A. Hinz, M.S. Seaman, F. Vanzetta, B.M. Fernandez-Rodriguez, C. Silacci, D. Pinna, D. Jarrossay, S. Balla-Jhagjhoorsingh, B. Willems, M.J. Zekveld, H. Dreja, E. O'Sullivan, C. Pade, C. Orkin, S.A. Jeffs, D.C. Montefiori, D. Davis, W. Weissenhorn, A. McKnight, J.L. Heeney, F. Sallusto, Q.J. Sattentau, R.A. Weiss, A. Lanzavecchia, Analysis of memory B cell responses and isolation of novel monoclonal antibodies with neutralizing breadth from HIV-1-infected individuals, PLoS One 5 (2010), e8805.
[18] D.C. Chan, C.T. Chutkowski, P.S. Kim, Evidence that a prominent cavity in the coiled coil of HIV type 1 gp41 is an

attractive drug target, Proc. Natl. Acad. Sci. U. S. A. 95 (1998) 15613–15617.
[19] F. Yu, L. Lu, L. Du, X. Zhu, A.K. Debnath, S. Jiang, Approaches for identification of HIV-1 entry inhibitors targeting gp41 pocket, Viruses 5 (2013) 127–149.
[20] E. Poveda, V. Briz, V. Soriano, Enfuvirtide, the first fusion inhibitor to treat HIV infection, AIDS Rev. 7 (2005) 139–147.
[21] M.L. Greenberg, N. Cammack, Resistance to enfuvirtide, the first HIV fusion inhibitor, J. Antimicrob. Chemother. 54 (2004) 333–340.
[22] L. Xu, A. Pozniak, A. Wildfire, S.A. Stanfield-Oakley, S.M. Mosier, D. Ratcliffe, J. Workman, A. Joall, R. Myers, E. Smit, P.A. Cane, M.L. Greenberg, D. Pillay, Emergence and evolution of enfuvirtide resistance following long-term therapy involves heptad repeat 2 mutations within gp41, Antimicrob. Agents Chemother. 49 (2005) 1113–1119.
[23] Y. He, J. Cheng, J. Li, Z. Qi, H. Lu, M. Dong, S. Jiang, Q. Dai, Identification of a critical motif for the human immunodeficiency virus type 1 (HIV-1) gp41 core structure: implications for designing novel anti-HIV fusion inhibitors, J. Virol. 82 (2008) 6349–6358.
[24] D.M. Eckert, P.S. Kim, Design of potent inhibitors of HIV-1 entry from the gp41 N-peptide region, Proc. Natl. Acad. Sci. U. S. A. 98 (2001) 11187–11192.
[25] J.M. Louis, C.A. Bewley, G.M. Clore, Design and properties of N(CCG)-gp41, a chimeric gp41 molecule with nanomolar HIV fusion inhibitory activity, J. Biol. Chem. 276 (2001) 29485–29489.
[26] J.M. Louis, I. Nesheiwat, L. Chang, G.M. Clore, C.A. Bewley, Covalent trimers of the internal N-terminal trimeric coiled-coil of gp41 and antibodies directed against them are potent inhibitors of HIV envelope-mediated cell fusion, J. Biol. Chem. 278 (2003) 20278–20285.
[27] M.J. Root, M.S. Kay, P.S. Kim, Protein design of an HIV-1 entry inhibitor, Science 291 (2001) 884–888.
[28] S. Crespillo, A. Camara-Artigas, S. Casares, B. Morel, E.S. Cobos, P.L. Mateo, N. Mouz, C.E. Martin, M.G. Roger, R. El Habib, B. Su, C. Moog, F. Conejero-Lara, Single-chain protein mimetics of the N-terminal heptad-repeat region of gp41 with potential as anti-HIV-1 drugs, Proc. Natl. Acad. Sci. U. S. A. 111 (2014) 18207–18212.
[29] C. Sabin, D. Corti, V. Buzon, M.S. Seaman, D. Lutje Hulsik, A. Hinz, F. Vanzetta, G. Agatic, C. Silacci, L. Mainetti, G. Scarlatti, F. Sallusto, R. Weiss, A. Lanzavecchia, W. Weissenhorn, Crystal structure and size-dependent neutralization properties of HK20, a human monoclonal antibody binding to the highly conserved heptad repeat 1 of gp41, PLoS Pathog. 6 (2010), e1001195.
[30] S.K. Sia, P.A. Carr, A.G. Cochran, V.N. Malashkevich, P.S. Kim, Short constrained peptides that inhibit HIV-1 entry, Proc. Natl. Acad. Sci. U. S. A. 99 (2002) 14664–14669.
[31] M.A. Luftig, M. Mattu, P. Di Giovine, R. Geleziunas, R. Hrin, G. Barbato, E. Bianchi, M.D. Miller, A. Pessi, A. Carfi, Structural basis for HIV-1 neutralization by a gp41 fusion intermediate-directed antibody, Nat. Struct. Mol. Biol. 13 (2006) 740–747.
[32] H.K. Steger, M.J. Root, Kinetic dependence to HIV-1 entry inhibition, J. Biol. Chem. 281 (2006) 25813–25821.
[33] K.M. Kahle, H.K. Steger, M.J. Root, Asymmetric deactivation of HIV-1 gp41 following fusion inhibitor binding, PLoS Pathog. 5 (2009), e1000674.
[34] K.W. Ahn, M.J. Root, Complex interplay of kinetic factors governs the synergistic properties of HIV-1 entry inhibitors, J. Biol. Chem. 292 (2017) 16498–16510.
[35] E. Bianchi, J.G. Joyce, M.D. Miller, A.C. Finnefrock, X. Liang, M. Finotto, P. Ingallinella, P. McKenna, M. Citron, E. Ottinger, R.W. Hepler, R. Hrin, D. Nahas, C. Wu, D. Montefiori, J.W. Shiver, A. Pessi, P.S. Kim, Vaccination with peptide mimetics of the gp41 prehairpin fusion intermediate yields neutralizing antisera against HIV-1 isolates, Proc. Natl. Acad. Sci. U. S. A. 107 (2010) 10655–10660.
[36] L. Cai, M. Gochin, A novel fluorescence intensity screening assay identifies new low-molecular-weight inhibitors of the gp41 coiled-coil domain of human immunodeficiency virus type 1, Antimicrob. Agents Chemother. 51 (2007) 2388–2395.
[37] S.G. Peisajovich, L. Blank, R.F. Epand, R.M. Epand, Y. Shai, On the interaction between gp41 and membranes: the immunodominant loop stabilizes gp41 helical hairpin conformation, J. Mol. Biol. 326 (2003) 1489–1501.
[38] A. deCamp, P. Hraber, R.T. Bailer, M.S. Seaman, C. Ochsenbauer, J. Kappes, R. Gottardo, P. Edlefsen, S. Self, H. Tang, K. Greene, H. Gao, X. Daniell, M. Sarzotti-Kelsoe, M.K. Gorny, S. Zolla-Pazner, C.C. LaBranche, J.R. Mascola, B.T. Korber, D.C. Montefiori, Global panel of HIV-1 Env reference strains for standardized assessments of vaccine-elicited neutralizing antibodies, J. Virol. 88 (2014) 2489–2507.
[39] Y.X. He, S.W. Liu, W.G. Jing, H. Lu, D.M. Cai, D.J. Chin, A.K. Debnath, F. Kirchhoff, S.B. Jiang, Conserved residue Lys (574) in the cavity of HIV-1 gp41 coiled-coil domain is critical for six-helix bundle stability and virus entry, J. Biol. Chem. 282 (2007) 25631–25639.
[40] M.Y. Leung, F.S. Cohen, Increasing hydrophobicity of residues in an anti-HIV-1 Env peptide synergistically improves potency, Biophys. J. 100 (2011) 1960–1968.
[41] Y. Deng, Q. Zheng, T.J. Ketas, J.P. Moore, M. Lu, Protein design of a bacterially expressed HIV-1 gp41 fusion inhibitor, Biochemistry 46 (2007) 4360–4369.
[42] J.L. Cole, V.M. Garsky, Thermodynamics of peptide inhibitor binding to HIV-1 gp41, Biochemistry 40 (2001) 5633–5641.
[43] M. Mink, S.M. Mosier, S. Janumpalli, D. Davison, L. Jin, T. Melby, P. Sista, J. Erickson, D. Lambert, S.A. Stanfield-Oakley, M. Salgo, N. Cammack, T. Matthews, M.L. Greenberg, Impact of human immunodeficiency virus type 1 gp41 amino acid substitutions selected during enfuvirtide treatment on gp41 binding and antiviral potency of enfuvirtide in vitro, J. Virol. 79 (2005) 12447–12454.
[44] D. Eggink, J.P. Langedijk, A.M. Bonvin, Y. Deng, M. Lu, B. Berkhout, R.W. Sanders, Detailed mechanistic insights into HIV-1 sensitivity to three generations of fusion inhibitors, J. Biol. Chem. 284 (2009) 26941–26950.
[45] M. Armand-Ugon, A. Gutierrez, B. Clotet, J.A. Este, HIV-1 resistance to the gp41-dependent fusion inhibitor C-34, Antivir. Res. 59 (2003) 137–142.
[46] B.E. McGillick, T.E. Balius, S. Mukherjee, R.C. Rizzo, Origins of resistance to the HIVgp41 viral entry inhibitor T20, Biochemistry 49 (2010) 3575–3592.
[47] Y. Lu, C.Y. Yang, S. Wang, Binding free energy contributions of interfacial waters in HIV-1 protease/inhibitor complexes, J. Am. Chem. Soc. 128 (2006) 11830–11839.
[48] A. Palencia, A. Camara-Artigas, M.T. Pisabarro, J.C. Martinez, I. Luque, Role of interfacial water molecules in proline-rich ligand recognition by the Src homology 3 domain of Abl, J. Biol. Chem. 285 (2010) 2823–2833.
[49] M.D. Khasnis, K. Halkidis, A. Bhardwaj, M.J. Root, Receptor activation of HIV-1 Env leads to asymmetric exposure of the gp41 trimer, PLoS Pathog. 12 (2016), e1006098.
[50] X.C. Ma, M.L. Lu, J. Gorman, D.S. Terry, X.Y. Hong, Z. Zhou, H. Zhao, R.B. Altman, J. Arthoe, S.C. Blanchard, P.D. Kwone,

J.B. Munro, W. Mothes, HIV-1 Env trimer opens through an asymmetric intermediate in which individual protomers adopt distinct conformations, Elife 7 (2018), e34271.
[51] E. Gasteiger, C. Hoogland, A. Gattiker, S.e. Duvaud, M.R. Wilkins, R.D. Appel, A. Bairoch, Protein identification and analysis tools on the ExPASy server, in: J.M. Walker (Ed.), The Proteomics Protocols Handbook, Humana Press, Totowa, NJ 2005, pp. 571–607.
[52] P. Luo, R.L. Baldwin, Mechanism of helix induction by trifluoroethanol: a framework for extrapolating the helix-forming properties of peptides from trifluoroethanol/water mixtures back to water, Biochemistry 36 (1997) 8413–8421.
[53] R. Lumry, H. Eyring, Conformation changes of proteins, J. Phys. Chem. 58 (1954) 110–120.
[54] A.A. McCarthy, R. Barrett, A. Beteva, H. Caserotto, F. Dobias, F. Felisaz, T. Giraud, M. Guijarro, R. Janocha, A. Khadrouche, M. Lentini, G.A. Leonard, M. Lopez Marrero, S. Malbet-Monaco, S. McSweeney, D. Nurizzo, G. Papp, C. Rossi, J. Sinoir, C. Sorez, J. Surr, O. Svensson, U. Zander, F. Cipriani, P. Theveneau, C. Mueller-Dieckmann, ID30B—a versatile beamline for macromolecular crystallography experiments at the ESRF, J. Synchrotron Radiat. 25 (2018) 1249–1260.
[55] C. Vonrhein, C. Flensburg, P. Keller, A. Sharff, O. Smart, W. Paciorek, T. Womack, G. Bricogne, Data processing and analysis with the autoPROC toolbox, Acta Crystallogr. D Biol. Crystallogr. 67 (2011) 293–302.
[56] P.R. Evans, An introduction to data reduction: space-group determination, scaling and intensity statistics, Acta Crystallogr. D Biol. Crystallogr. 67 (2011) 282–292.
[57] Collaborative Computational Project, N, The CCP4 suite: programs for protein crystallography, Acta Crystallogr. D Biol. Crystallogr. 50 (1994) 760–763.
[58] P.D. Adams, P.V. Afonine, G. Bunkoczi, V.B. Chen, I.W. Davis, N. Echols, J.J. Headd, L.W. Hung, G.J. Kapral, R.W. Grosse-Kunstleve, A.J. McCoy, N.W. Moriarty, R. Oeffner, R.J. Read, D.C. Richardson, J.S. Richardson, T.C. Terwilliger, P.H. Zwart, PHENIX: a comprehensive Python-based system for macromolecular structure solution, Acta Crystallogr. D Biol. Crystallogr. 66 (2010) 213–221.
[59] G. Bunkoczi, N. Echols, A.J. McCoy, R.D. Oeffner, P.D. Adams, R.J. Read, Phaser.MRage: automated molecular replacement, Acta Crystallogr. D Biol. Crystallogr. 69 (2013) 2276–2286.
[60] P. Emsley, K. Cowtan, Coot: model-building tools for molecular graphics, Acta Crystallogr. D Biol. Crystallogr. 60 (2004) 2126–2132.
[61] P. Emsley, B. Lohkamp, W.G. Scott, K. Cowtan, Features and development of Coot, Acta Crystallogr. D Biol. Crystallogr. 66 (2010) 486–501.
[62] P.V. Afonine, R.W. Grosse-Kunstleve, N. Echols, J.J. Headd, N.W. Moriarty, M. Mustyakimov, T.C. Terwilliger, A. Urzhumtsev, P.H. Zwart, P.D. Adams, Towards automated crystallographic structure refinement with phenix.refine, Acta Crystallogr. D Biol. Crystallogr. 68 (2012) 352–367.
[63] V.B. Chen, W.B. Arendall 3rd, J.J. Headd, D.A. Keedy, R.M. Immormino, G.J. Kapral, L.W. Murray, J.S. Richardson, D.C. Richardson, MolProbity: all-atom structure validation for macromolecular crystallography, Acta Crystallogr. D Biol. Crystallogr. 66 (2010) 12–21.
[64] R.A. Laskowski, PDBsum: summaries and analyses of PDB structures, Nucleic Acids Res. 29 (2001) 221–222.
[65] I. Luque, O.L. Mayorga, E. Freire, Structure-based thermodynamic scale of alpha-helix propensities in amino acids, Biochemistry 35 (1996) 13681–13688.
[66] B. Lee, F.M. Richards, The interpretation of protein structures: estimation of static accessibility, J. Mol. Biol. 55 (1971) 379–400.
[67] J. Gomez, V.J. Hilser, D. Xie, E. Freire, The heat capacity of proteins, Proteins 22 (1995) 404–412.
[68] V.J. Hilser, J. Gomez, E. Freire, The enthalpy change in protein folding and binding: refinement of parameters for structure-based calculations, Proteins 26 (1996) 123–133.
[69] M. Sarzotti-Kelsoe, R.T. Bailer, E. Turk, C.L. Lin, M. Bilska, K.M. Greene, H. Gao, C.A. Todd, D.A. Ozaki, M.S. Seaman, J.R. Mascola, D.C. Montefiori, Optimization and validation of the TZM-bl assay for standardized assessments of neutralizing antibodies against HIV-1, J. Immunol. Methods 409 (2014) 131–146.
[70] L.T. Rimsky, D.C. Shugars, T.J. Matthews, Determinants of human immunodeficiency virus type 1 resistance to gp41-derived inhibitory peptides, J. Virol. 72 (1998) 986–993.